fluids

MDPI

Article

MCV-Driven Effective Viscosity Modulation and Its Hemodynamic Impact in an Idealized Carotid Bifurcation: A Computational Fluid Dynamics Study

Arif Çutay *, Hakan Bayrakcı, Özdeş Çermik and Muharrem İmal

Department of Mechanical Engineering, Kahramanmaraş Sütçü İmam University, 46040 Kahramanmaraş, Türkiye; bayrakcihakan046@gmail.com (H.B.); ozdescermik@ksu.edu.tr (Ö.Ç.); muharremimal@ksu.edu.tr (M.İ.)

* Correspondence: arifcutay@ksu.edu.tr; Tel.: +90-344-300-45-88

Abstract

Mean corpuscular volume (*MCV*) is a routinely measured hematological parameter that influences blood viscosity by altering red blood cell volume and packing density. Although *MCV* is physiologically linked to hemorheological behavior, to the authors' knowledge, its direct role in modulating large-artery hemodynamics has not been systematically quantified. This study introduces an *MCV*-driven effective Newtonian viscosity mode to evaluate the first-order impact of *MCV* variation on carotid bifurcation flow. Rather than employing shear-dependent constitutive laws, blood viscosity was scaled through an *MCV*-based formulation, yielding three Newtonian fluids corresponding to clinically relevant *MCV* levels of 70, 90, and 110 fL. Pulsatile CFD simulations were performed in four idealized carotid bifurcation geometries (40°, 50°, 65°, and 100°) to assess the combined influence of vascular geometry and *MCV*-dependent viscosity variation. Hemodynamic indices including time-averaged wall shear stress (TAWSS), oscillatory shear index (OSI), and relative residence time (RRT) were quantified, and a two-way analysis of variance (ANOVA) was employed to distinguish the relative contributions of geometric configuration and *MCV*. Across the investigated *MCV* range, increasing *MCV* produced a geometry-dependent modulation of shear-based indices, with TAWSS increasing by up to approximately 11%, while OSI and RRT decreased by about 20–25% and 10%, respectively, particularly in geometries exhibiting pronounced flow separation. Although vascular geometry remained the dominant determinant of overall hemodynamic patterns, *MCV*-induced viscosity scaling significantly modulated low-shear and recirculation regions. These findings suggest that *MCV*-dependent viscosity scaling can complement patient-specific hemodynamic assessments and provide a rational baseline for future shear-dependent and personalized rheological modeling frameworks.

Keywords: mean corpuscular volume; effective viscosity; Newtonian model; carotid bifurcation; hemodynamics; computational fluid dynamics

Check for updates

Academic Editors: Xing Zhang, Chengcheng Tao and Mehrdad Massoudi

Received: 4 December 2025
Revised: 17 January 2026
Accepted: 26 January 2026
Published: 29 January 2026

Copyright: © 2026 by the authors. Licensee MDPI, Basel, Switzerland. This article is an open access article distributed under the terms and conditions of the Creative Commons Attribution (CC BY) license.

1. Introduction

Hemodynamic forces play a central role in the initiation and progression of atherosclerotic disease, particularly at arterial branching sites such as the carotid bifurcation. Shear-based indices including wall shear stress (WSS), oscillatory shear index (OSI), and relative residence time (RRT) are widely used to characterize disturbed-flow environments associated with endothelial dysfunction and plaque susceptibility. Numerous computational

fluid dynamics (CFD) studies have demonstrated that these indices are influenced by vascular geometry, pulsatile flow conditions, and the rheological description of blood. Despite this, most idealized and patient-specific carotid simulations continue to rely on constant-viscosity Newtonian blood models, motivated by numerical robustness and the assumption that shear-dependent rheological effects primarily manifest at the microcirculatory scale.

Blood viscosity is governed by multiple hematological factors, including hematocrit, red blood cell (RBC) aggregation, and RBC deformability. Mean corpuscular volume (MCV) is a routinely measured clinical parameter that reflects average RBC volume and is indirectly related to cell packing density and baseline viscosity. Abnormal MCV values occur in a wide range of physiological and pathological conditions; however, the potential influence of MCV variation on large-artery hemodynamics has not yet been systematically investigated.

Previous experimental, numerical, and imaging-based studies have consistently shown that carotid bifurcation hemodynamics are predominantly governed by vascular geometry, with parameters such as bifurcation angle, bulb morphology, and curvature strongly influencing flow separation, recirculation zones, and shear heterogeneity. While inlet conditions and boundary modeling affect local flow features, geometric configuration remains the dominant determinant of disturbed-flow exposure in arterial bifurcations, providing a well-defined baseline against which secondary modulatory effects may be assessed.

Hemodynamic behavior in the carotid bifurcation is strongly governed by geometric features such as bifurcation angle, curvature, and bulb enlargement. Numerous CFD studies have demonstrated that these structural parameters dictate the formation of disturbed-flow regions and the distribution of shear-related hemodynamic indices. Campbell et al. [1] showed that although inlet velocity profiles modulate local WSS and OSI, geometric fidelity remains the dominant factor shaping flow patterns. Moyle et al. [2] similarly reported that secondary and helical flow components decay rapidly within a few vessel diameters and account for less than 15% of WSS variability, whereas geometric morphology explains nearly half of the variation. The influence of outlet boundary conditions has also been examined; Morbiducci et al. [3] demonstrated that physiologic time-varying outflow ratios reduce temporal WSS oscillations but preserve the spatial distribution, further underscoring the geometric control of flow. Geometric descriptors such as proximal area ratio and bifurcation tortuosity were identified as statistically significant predictors of disturbed-flow exposure and atherosclerosis susceptibility, whereas bifurcation angle and planarity showed limited association [4]. Geometric descriptors such as proximal area ratio, bifurcation tortuosity, and bulb diameter have been identified as significant predictors of low-WSS exposure and atherosclerosis susceptibility [4–6]. MRI-based patient-specific analyses support these findings, showing that variations in bulb eccentricity and curvature substantially influence WSS, OSI, and recirculation strength [7,8]. Idealized-model investigations by Antiga et al. [9] further revealed that even modest changes in bifurcation angle or outflow area ratio produce large differences in jet impingement, separation length, and near-wall shear gradients. Sensitivity analyses by Lee and Steinman [10] confirmed that geometry plays a substantially larger role than inlet profile, pulsatility index, or wall compliance in determining bifurcation hemodynamics. Complementary in-vivo 4D-flow MRI investigations confirmed that regions of low WSS and elevated OSI typically localize near the carotid bulb and are modulated by bifurcation geometry and mild stenosis, returning toward normal after surgical revascularization [11]. Longitudinal MRI-based cohort studies further indicated that enlarged internal carotid bulb diameter, wide bifurcation angle, and persistently low WSS act as independent predictors of atherosclerotic wall thickening, while tortuosity exerts a protective influence [7]. Collectively, these findings emphasize that accurate carotid hemodynamic prediction demands high-fidelity geometric

reconstruction, physiologic boundary modeling, and advanced numerical or data-driven frameworks to link local flow behavior with clinical vascular risk.

Classical hemorheological studies have long established erythrocyte volume as a key determinant of blood viscosity. Chien demonstrated that effective cell volume strongly governs low-shear viscosity, directly linking red blood cell (RBC) size to bulk rheological behavior [12]. Similarly, Skalak and Brånemark reported that erythrocyte size and deformability significantly influence microvascular resistance, underscoring the mechanistic role of cell morphology in modulating apparent viscosity [13]. Comprehensive reviews by Popel and Johnson further emphasized that hematocrit, erythrocyte volume, aggregation, and deformability jointly shape macroscopic viscosity across physiological and pathological states [14].

Building upon this classical framework, recent studies have explicitly linked geometry-induced disturbed flow formation with hemorheological effects under both physiologic and pathological conditions. Contemporary reviews and large-cohort CFD investigations demonstrate that complex vascular geometries—including bifurcations, curvature, stenosis, and post-stenotic dilatation—systematically generate recirculation zones, vortical structures, and helical flow patterns that promote low and oscillatory wall shear stress (WSS) environments [15–18]. Importantly, disturbed-flow exposure is governed not only by bifurcation angle but also by diameter ratio, bulb eccentricity, tortuosity, and surface irregularities, with excessive geometric smoothing shown to suppress vortical structures and underestimate WSS heterogeneity [19,20].

Parallel advances in hemorheology-aware modeling have clarified how blood rheology modulates geometry-driven disturbed flow. While several large-vessel studies report minor differences between Newtonian and shear-thinning models in regions of high shear [21], recent evidence indicates that abnormal hemorheological conditions—such as altered hematocrit, enhanced erythrocyte aggregation, and yield-stress behavior—significantly amplify low-WSS, high oscillatory shear index (OSI), and elevated relative residence time (RRT), particularly in bifurcated and stenotic geometries [22,23]. Moreover, numerical and experimental investigations under pulsatile and Womersley flow conditions reveal that axial shear rate and flow unsteadiness play a critical role in coupling vascular geometry with micro-scale rheological effects, especially in regions of flow separation and secondary motion [24,25].

Collectively, these findings indicate that accurate prediction of carotid hemodynamics requires consideration of both vascular geometry and blood rheology. While geometric complexity is widely recognized as the dominant determinant of flow separation and shear heterogeneity in arterial bifurcations, secondary rheological factors may modulate disturbed-flow patterns, particularly in regions exposed to low and oscillatory shear.

Despite extensive investigation of shear-rate- and hematocrit-dependent blood rheology, the contribution of mean corpuscular volume (MCV) has not yet been explicitly incorporated into arterial-scale hemodynamic simulations. Consequently, the isolated influence of MCV variation on shear-based hemodynamic indices in geometrically complex regions such as the carotid bifurcation remains insufficiently explored.

In this context, the present manuscript introduces a parametric CFD framework that explicitly accounts for MCV-dependent blood viscosity while systematically examining its interaction with carotid bifurcation geometry. By isolating the role of erythrocyte volume within a simplified Newtonian viscosity scaling approach, this study uniquely contributes by quantifying the first-order effects of MCV on TAWSS, OSI, and RRT under physiologically realistic pulsatile flow conditions.

2. Materials and Methods

2.1. Geometric Model

A three-dimensional model of the human carotid bifurcation was constructed to represent four different bifurcation angles corresponding to physiologically observed variations in vascular geometry. The baseline geometry, schematically illustrated in Figures 1 and 2, was derived from an idealized carotid artery configuration consisting of the common carotid artery (CCA), internal carotid artery (ICA), and external carotid artery (ECA). In the schematic model, D_1 denotes the inlet section corresponding to the CCA, while D_3 and D_4 represent the outlets of the ICA and ECA, respectively. The region labeled D_2 identifies the bifurcation zone, and the angle θ defines the geometric divergence between the two daughter branches.

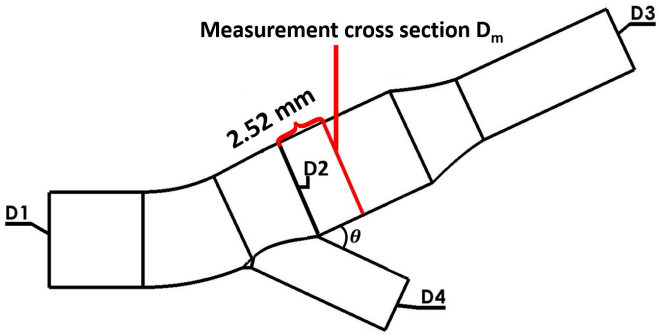
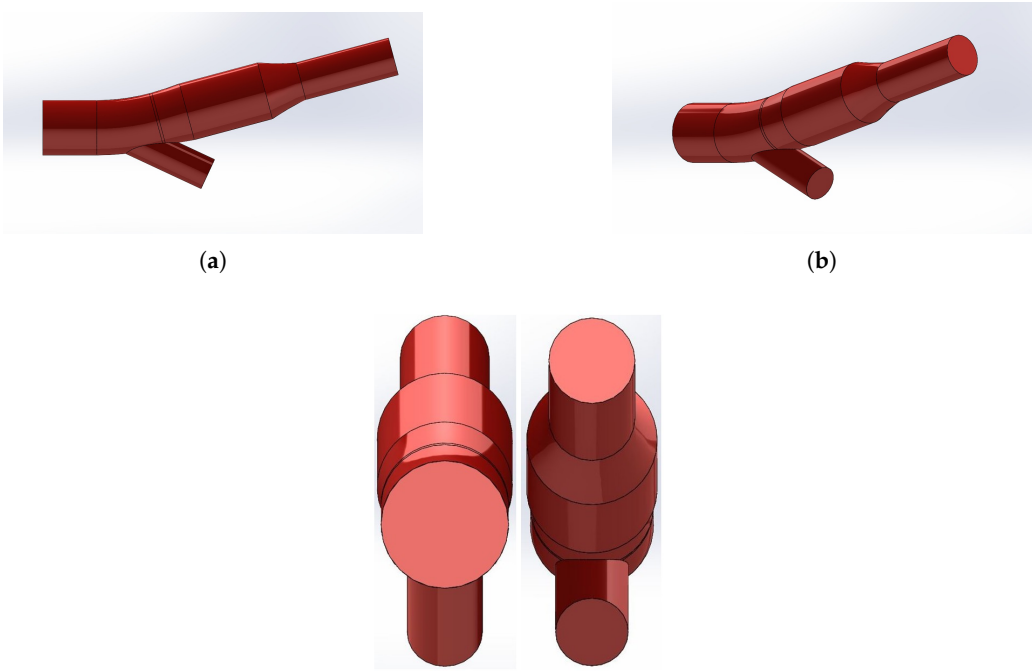


Figure 1. Schematic representation of the carotid bifurcation model showing the inlet (D1), bifurcation zone (D2), and outlets (D3: ICA, D4: ECA).



(**a**) (**b**)

(**c**)

Figure 2. Different viewing orientations of the constructed three-dimensional carotid bifurcation model: (**a**) front view, (**b**) perspective view, (**c**) inlet and outlets views. The multiple perspectives highlight the geometric continuity and curvature transitions between the inlet (D1), bifurcation region (D2), and outlets (D3: ICA, D4: ECA).

The bifurcation angle θ was parametrically varied as 40°, 50°, 65°, and 100° to investigate the influence of geometric divergence on flow distribution and wall shear stress (WSS).

These angles were selected to span a broad range of geometrical configurations commonly employed in idealized carotid bifurcation studies. Previous experimental and computational investigations have demonstrated that variations in bifurcation angle strongly influence flow separation, secondary flow development, and near-wall shear patterns, particularly in the vicinity of the flow divider [26–28]. Accordingly, moderate angles (40–65°) were used to represent physiological flow division, while a highly divergent configuration (100°) was included to deliberately induce disturbed flow conditions and enhance hemodynamic sensitivity to geometric effects.

The characteristic dimensions of the model were adopted from the well-established carotid bifurcation geometries proposed by Perktold et al. [29], which have been extensively validated against experimental flow measurements. Accordingly, the diameters were set to $D_1 = 6.20$ mm, $D_2 = 6.32$ mm, $D_3 = 4.34$ mm, and $D_4 = 3.66$ mm to ensure dimensional consistency with human carotid anatomy.

2.2. Governing Equations

Blood flow was governed by the incompressible continuity and Navier–Stokes equations:

$$\nabla \cdot \mathbf{u} = 0,$$

$$\rho\left(\frac{\partial \mathbf{u}}{\partial t} + \mathbf{u} \cdot \nabla \mathbf{u}\right) = -\nabla p + \nabla \cdot \left[\mu_{\text{eff}}(\text{MCV})\left(\nabla \mathbf{u} + \nabla \mathbf{u}^T\right)\right],$$

where $\mathbf{u}$ denotes the velocity field, p is the pressure, and μ_{eff} represents the MCV-dependent effective viscosity model

Blood was modeled as a Newtonian fluid whose effective viscosity is modulated by the MCV. Although blood exhibits shear-thinning behavior at low shear rates, several studies have demonstrated that a Newtonian assumption yields sufficiently accurate hemodynamic predictions in large arteries where shear rates typically exceed 100 s^{-1} [21,30–33]. This simplification enables a controlled assessment of how erythrocyte-volume variability modulates bulk viscosity without introducing the confounding effects of shear-rate-dependent constitutive models.

The rationale for incorporating MCV arises from classical hemorheological findings showing that erythrocyte volume, deformability, and packing density modulate effective viscosity [12–14]. Larger erythrocytes increase the effective hematocrit and reduce cell–cell spacing, thereby elevating low-shear viscosity, whereas smaller erythrocytes have the opposite effect. Experimental studies by Baskurt and Meiselman [34] and Cokelet and Meiselman [35] further confirm that morphological variations in erythrocytes can alter bulk viscosity independently of shear rate. Despite this evidence, hemorheological models used in large-artery CFD almost exclusively rely on hematocrit or shear rate and do not explicitly incorporate erythrocyte-volume effects.

To quantify the first-order influence of MCV on viscosity, an effective Newtonian scaling law was adopted:

$$\mu_{\text{eff}}(MCV) = \mu_0\left[1 + \alpha\left(\frac{MCV - MCV_{\text{ref}}}{MCV_{\text{ref}}}\right)\right], \quad (1)$$

where $\mu_0 = 3.5 \times 10^{-3}$ Pa · s is the baseline viscosity and $MCV_{\text{ref}} = 90$ fL represents a typical adult reference value.

The empirical sensitivity coefficient, $\alpha = 0.015$, was introduced as a phenomenological parameter for sensitivity analysis rather than as an experimentally calibrated material constant. Its value was selected to satisfy two criteria: (i) ensuring that the viscosity–MCV slope remains broadly consistent with experimental trends reported for hematocrit-

and morphology-driven viscosity variation [14,34], and (ii) producing physiologically realistic viscosity changes (approximately ±8% across 70–110 fL), comparable to variations observed under macrocytic and microcytic hematological conditions. Accordingly, α acts as a morphology-weighting factor that captures the increase in apparent viscosity associated with macrocytosis (MCV $>$ 90 fL) and the decrease associated with microcytosis (MCV $<$ 90 fL).

It is emphasized that the proposed scaling law is intended as a proof-of-concept formulation rather than a general rheological theory. Because erythrocyte volume, hematocrit, and red blood cell deformability are physiologically interdependent, the present model cannot fully disentangle the isolated contribution of MCV from concurrent changes in cell concentration or membrane mechanics. Instead, MCV is treated as an effective proxy variable that modulates bulk viscosity through changes in packing density and cell spacing, enabling a controlled assessment of first-order morphology-driven viscosity effects in large-artery CFD simulations.

Because the model is Newtonian and time-invariant, each simulation was performed using a constant viscosity corresponding to the selected MCV group without any cell-wise rheological update. The resulting effective viscosities were:

$$\begin{aligned} MCV = 70 \text{ fL} \quad &\Rightarrow \quad \mu_{\text{eff}} = 3.23 \times 10^{-3} \text{ Pa} \cdot \text{s}, \\ MCV = 90 \text{ fL} \quad &\Rightarrow \quad \mu_{\text{eff}} = 3.50 \times 10^{-3} \text{ Pa} \cdot \text{s}, \\ MCV = 110 \text{ fL} \quad &\Rightarrow \quad \mu_{\text{eff}} = 3.78 \times 10^{-3} \text{ Pa} \cdot \text{s}. \end{aligned}$$

This formulation provides a physiologically informed yet computationally lightweight framework for isolating the first-order rheological effect of erythrocyte volume on large-artery hemodynamics. By avoiding shear-dependent models, the approach allows direct attribution of viscosity-related hemodynamic changes to MCV variation alone, which is particularly advantageous for evaluating morphology-driven hemodynamic sensitivity in geometrically complex regions such as the carotid bifurcation.

2.3. Boundary Conditions

A physiologically realistic pulsatile inlet velocity waveform was adopted from the benchmark study of Bharadvaj et al. [36] and imposed at the common carotid artery (CCA). The waveform shown in Figure 3 is presented in normalized form, consistent with its original representation in the reference study, and therefore does not imply a specific Reynolds number. The normalized time formulation preserves the waveform shape independently of the absolute heart rate.

For the numerical simulations, this normalized waveform was subsequently dimensionalized and uniformly scaled such that the resulting cycle-averaged flow corresponds to a Reynolds number of Re $=$ 300, representing physiologically realistic resting-flow conditions in the human common carotid artery. This approach retains the temporal characteristics of the benchmark waveform while enforcing the desired mean flow level.

The inlet velocity was prescribed as a temporally varying but spatially uniform (plug) profile. The imposed velocity scaling and cardiac cycle period ensure mutual consistency between the Reynolds and Womersley numbers. Under the present conditions, the resulting flow corresponds to a Womersley number of $\alpha = 4.28$, confirming the presence of significant unsteady inertial effects representative of physiological carotid artery flow. The selected Reynolds and Womersley numbers fall within the physiological range commonly reported for human carotid arteries under resting conditions.

At the internal (ICA) and external carotid artery (ECA) outlets, a three-element Windkessel (RCR) model was employed to represent the downstream vascular impedance. The proximal resistance (R_1) accounts for characteristic impedance effects and controls high-

frequency wave reflections, whereas the distal resistance (R_2) represents peripheral vascular resistance and was adjusted to achieve physiologically realistic mean flow partitioning between the ICA and ECA. The compliance parameter (C) was selected to reproduce physiological pressure damping and the phase lag between pressure and flow. The total resistance ($R_1 + R_2$) was calibrated to ensure numerical stability and realistic pressure levels under pulsatile inflow conditions.

All arterial walls were assumed rigid and treated with a no-slip boundary condition. Blood was modeled as an incompressible fluid, and gravitational effects were neglected.

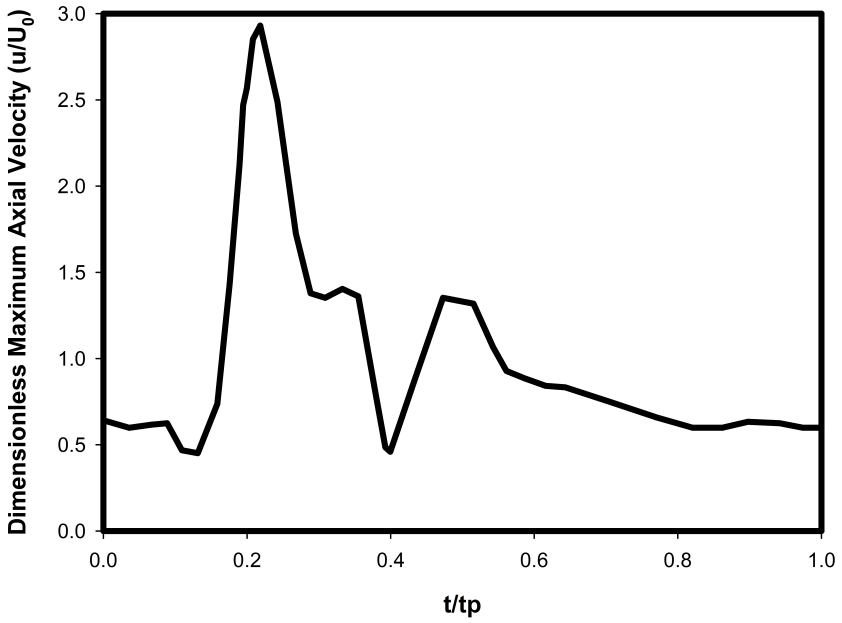


Figure 3. Normalized pulsatile inlet velocity waveform imposed at the common carotid artery (CCA) based on the profile reported by Bharadvaj et al. [36]. The velocity magnitude is prescribed as a function of the normalized time t/t_p and applied as a spatially uniform (plug) profile over the inlet cross-section.

2.4. Solver Settings

All simulations were performed in ANSYS Fluent 2021 R2 using the pressure-based solver with the COUPLED pressure–velocity algorithm. Spatial discretization employed the least-squares cell-based method for gradient evaluation. Pressure was discretized using a second-order scheme, while the momentum equations were treated with a second-order upwind formulation. Time integration was carried out using a second-order implicit scheme with a fixed time step of $\Delta t = 1 \times 10^{-3}$ s.

A time-step sensitivity analysis was conducted by comparing key hemodynamic quantities, including maximum axial velocity and surface-averaged time-averaged wall shear stress (TAWSS), using progressively refined time steps. Three time steps were examined, and differences between $\Delta t = 1 \times 10^{-3}$ s and the two finer time steps remained below 1% for both monitored quantities. Accordingly, $\Delta t = 1 \times 10^{-3}$ s was selected as an optimal compromise between temporal accuracy and computational efficiency.

Convergence at each physical time step was ensured by reducing the scaled residuals for continuity and momentum equations below 10^{-6}. In addition to residual monitoring, global flow quantities including inlet mass flow rate, ICA/ECA outlet flow partition ratio, and instantaneous pressure drop were continuously tracked to ensure numerical stability.

The computational mesh was generated using ANSYS Meshing, consisting of an unstructured hybrid grid with tetrahedral elements and locally refined prism layers near the arterial wall. To eliminate transient start-up artifacts, each simulation was advanced

for three cardiac cycles prior to data extraction. Periodicity was verified by comparing the maximum axial velocity and surface-averaged TAWSS between successive cycles, with variations remaining below 1%. All hemodynamic metrics were therefore computed from the fourth cardiac cycle after periodic convergence had been established.

Simulations were executed on a workstation equipped with an AMD Ryzen 9 5950X processor (16 physical cores, 32 logical threads) and 64 GB of RAM using shared-memory parallel computation. The total computational time for a single simulation case, corresponding to four cardiac cycles, was approximately 8–10 h, depending on convergence behavior and rheological model selection.

A total of twelve simulations were performed by combining three *MCV*-dependent viscosity conditions (70, 90, and 110 fL) with the four bifurcation geometries introduced in Section 2.1. For each configuration, near-wall hemodynamics were quantified using time-integrated wall shear stress fields over one cardiac cycle. Instantaneous WSS values extracted at every wall node were first integrated over the full pulsatile period and subsequently surface-averaged across the luminal boundary, yielding a single representative scalar value for each index per simulation—an essential requirement for statistical comparison and ANOVA. Post-processing and streamline visualization were conducted in ANSYS CFD-Post to assess how geometric divergence and *MCV*-driven viscosity modulation collectively influence local flow organization and recirculation behavior. Table 1 provides the mathematical definitions of the three hemodynamic indices: TAWSS, which measures the cycle-averaged shear magnitude; OSI, which quantifies directional shear oscillations; and RRT, which reflects the combined effect of low and oscillatory shear associated with prolonged near-wall residence. Together, these indices offer complementary insight into flow stability and regions susceptible to atherogenic conditions.

The instantaneous wall shear stress $\tau_w(t)$ was obtained directly from the CFD solution as the tangential shear stress acting on the vessel wall and computed from the local velocity gradient normal to the wall. Specifically, $\tau_w(t)$ was evaluated at each wall-adjacent node as

$$\tau_w(\boldsymbol{x}, t) = \left\| \mu_{\text{eff}}(\dot{\gamma}, t) \left. \frac{\partial \boldsymbol{u}_t}{\partial n} \right|_{\boldsymbol{x}} \right\|, \tag{2}$$

where $\boldsymbol{u}_t$ denotes the tangential velocity component, n is the wall-normal direction, and μ_{eff} represents the effective dynamic viscosity governed by the local *MCV*-dependent rheological model. The time-resolved $\tau_w(\boldsymbol{x}, t)$ field was first integrated over one cardiac cycle of duration T at each wall location to compute the local TAWSS. Subsequently, a global surface-averaged value was obtained by averaging over the entire luminal wall surface, excluding the inlet and outlet cross-sectional boundaries. This procedure yields a single representative scalar value per hemodynamic index and simulation case, which is required for statistical comparison and ANOVA.

Table 1. Time-integrated definitions of the hemodynamic indices computed over one cardiac cycle T. All quantities were evaluated at each wall node and then surface-averaged.

Index	Expression
Time-Averaged Wall Shear Stress (TAWSS)	$\text{TAWSS} = \frac{1}{T} \int_0^T \lvert \boldsymbol{\tau}_w(t) \rvert \, dt$
Oscillatory Shear Index (OSI)	$\text{OSI} = \frac{1}{2} \left(1 - \frac{\left\lvert \int_0^T \boldsymbol{\tau}_w(t) \, dt \right\rvert}{\int_0^T \lvert \boldsymbol{\tau}_w(t) \rvert \, dt} \right)$
Relative Residence Time (RRT)	$\text{RRT} = \frac{1}{(1 - 2\,\text{OSI})\,\text{TAWSS}}$

2.5. Mesh Generation and Independence Study

An unstructured hybrid mesh was generated for the carotid bifurcation models to accurately resolve both near-wall and core flow dynamics. As illustrated in Figure 4, mesh refinement was concentrated in the bifurcation region, particularly around the flow divider and along the inner curvature of the internal carotid artery, where steep velocity and wall shear stress gradients are expected. The near-wall region was resolved using 12 prism layers, with the first-layer thickness selected to achieve a non-dimensional wall distance of $y^+ < 1$. A growth rate of 1.15 was applied between successive layers to ensure a smooth transition from the boundary-layer mesh to the tetrahedral core, thereby minimizing abrupt element-size changes and excessive cell skewness.

To assess the sensitivity of the numerical solution to spatial discretization, a mesh independence study was conducted on the reference geometry (Model B) using three systematically refined meshes. The total number of elements was increased with an approximately uniform multiplicative refinement ratio of two between successive levels, resulting in meshes containing approximately 5.0×10^5, 1.0×10^6, and 2.0×10^6 elements. This refinement strategy provides a clear definition of the grid refinement ratio and enables a rigorous evaluation of grid convergence in accordance with standard numerical verification protocols.

Mesh convergence was evaluated using two representative hemodynamic metrics: (1) the peak systolic axial velocity magnitude at point D_m, located near the flow divider where velocity gradients are highest, and (2) the surface-averaged time-averaged wall shear stress (TAWSS), computed over one cardiac cycle by averaging the local time-integrated wall shear stress over the entire luminal wall surface, excluding the inlet and outlet cross-sectional boundaries. These quantities were selected to capture both localized high-gradient behavior and global wall shear characteristics.

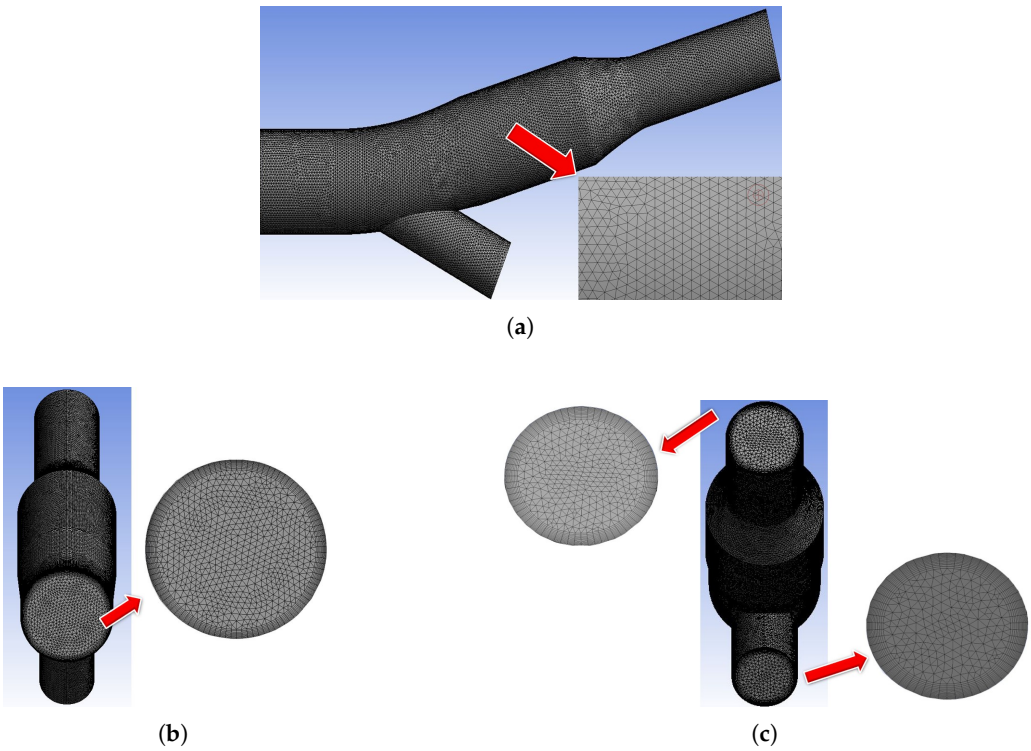
The variation of peak systolic axial velocity and cycle-averaged TAWSS with increasing mesh resolution is shown in Figure 5, respectively. Both metrics exhibit a clear convergence trend, with substantial changes observed between the coarse and medium meshes, followed by only minor variations between the medium and fine meshes. Specifically, the difference between the 1.0×10^6- and 2.0×10^6-element meshes remained below 0.5% for peak systolic velocity and below 1.0% for cycle-averaged TAWSS, indicating practical grid convergence for the quantities of interest.

To further quantify spatial discretization uncertainty, a Grid Convergence Index (GCI) analysis was performed following Roache's formulation. The three meshes were treated as coarse, medium, and fine levels to estimate the apparent order of accuracy and the associated fine–medium (GCI_{21}) and medium–coarse (GCI_{32}) indices. For both monitored quantities, GCI_{21} values were on the order of 1% or less, while GCI_{32} values were higher, consistent with the expected reduction in discretization error under systematic refinement. The ratio $GCI_{21} / (GCI_{32} r^p)$ was close to unity, indicating that the solutions approach the asymptotic range of grid convergence.

Because the employed viscosity model is Newtonian and independent of local shear rate, mesh sensitivity was not affected by variations in MCV-dependent viscosity. Accordingly, the mesh containing approximately 1.0×10^6 elements was selected for all simulations as an optimal compromise between numerical accuracy and computational cost. Temporal discretization effects were independently assessed through a time-step sensitivity analysis, as detailed in the Solver Settings Section.

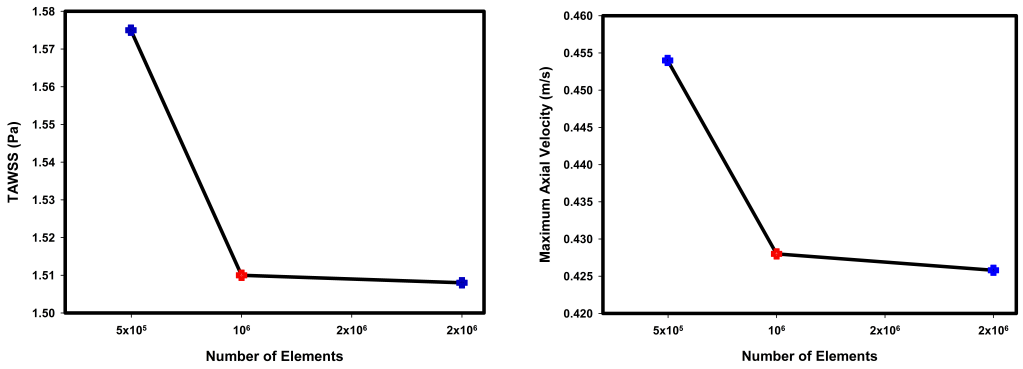
Table 2 summarizes the mesh quality parameters obtained for all four carotid bifurcation geometries (A–D). All meshes exhibit acceptable overall quality, with maximum skewness values below 0.68 and minimum orthogonal quality above 0.18, which fall within recommended limits for CFD simulations in vascular domains. Minor variations among the geometries reflect differences in bifurcation angle and curvature, while the overall

mesh uniformity confirms that the generated meshes are sufficiently accurate for hemodynamic analysis.



(**a**) (**b**) (**c**)

Figure 4. Mesh structure and near-wall refinement of the bifurcation model: (**a**) global mesh and magnified view of the critical region, (**b**) inlet mesh structure, and (**c**) outlet mesh structure.



(**a**) Cycle-averaged TAWSS (**b**) Peak systolic velocity

Figure 5. Mesh independence analysis based on cycle-averaged TAWSS and peak systolic velocity. The red marker indicates the selected mesh resolution adopted for all subsequent simulations.

Table 2. Mesh quality parameters for different carotid bifurcation geometries.

Geometry	Max Skewness	Min Orthogonal Quality	Average Element Quality
A	0.6746	0.1841	0.4658
B	0.6548	0.1958	0.4671
C	0.6630	0.2221	0.4611
D	0.6698	0.2075	0.4625

2.6. Model Validation

The numerical framework was validated against the benchmark study of Perktold and Resch [37], who reported phase-averaged velocity and wall shear stress distributions for pulsatile flow in a three-dimensional carotid bifurcation. Validation focused on both the temporal evolution of axial velocity and the spatial distribution of wall shear stress (WSS), ensuring consistency in unsteady flow dynamics and near-wall hemodynamic behavior.

Velocity-based validation was performed using the nondimensional maximum axial velocity extracted at the common carotid artery inlet at multiple normalized time instants (t/t_p) over one cardiac cycle. In accordance with the benchmark study, the axial velocity was nondimensionalized using the mean inlet velocity U_0, such that the dimensionless velocity is expressed as u/U_0. Time was normalized by the cardiac cycle period t_p, following the normalization adopted in the reference data.

The sampling location, denoted as point D_m in the present geometry, corresponds to a centerline-adjacent point within the mid-sinus region where the axial velocity attains its maximum value during systole and is therefore highly sensitive to the accuracy of the imposed inlet waveform and temporal resolution.

Figure 6 compares the temporal evolution of the nondimensional maximum axial velocity predicted by the present model with the benchmark results. Excellent agreement is observed throughout the cardiac cycle. The maximum deviation at peak systole ($t/t_p = 0.22$) remained below 3.2%, while the phase shift of the systolic maximum did not exceed $\Delta(t/t_p) = 0.015$. Furthermore, a quantitative comparison based on the normalized L_2 error norm of the axial velocity signal yielded a discrepancy below 4%, which lies well within commonly accepted validation limits for large-artery CFD simulations.

In addition to velocity validation, the predicted wall shear stress distribution was qualitatively and quantitatively compared with the reference results at peak systole ($t/t_p = 0.22$). The present simulations successfully reproduce a distinct local minimum in WSS along the non-dividing wall near the flow divider, consistent with the separation-prone region reported in the benchmark study. Downstream of the carotid sinus, elevated WSS levels of the same order of magnitude as the reference data (approximately 6–8 $\mathrm{N/m^2}$) are observed, indicating accurate recovery of near-wall momentum following flow separation.

Moreover, the computed location of the stagnation point at the tip of the dividing wall and the subsequent downstream redistribution of WSS along the dividing surface closely match the trends reported in the benchmark results. These observations confirm that the present model captures not only the temporal characteristics of pulsatile flow but also the spatial organization of shear-related hemodynamic features that are critical for bifurcation flow validation.

The slightly higher velocity magnitudes observed in the present simulations are primarily attributed to the deliberate scaling of the inlet waveform to a physiologically representative Reynolds number ($\mathrm{Re} = 300$) and Womersley number ($\alpha = 4.28$), rather than to a direct amplitude-matched replication of the benchmark inflow conditions. Minor discrepancies in peak amplitude and timing can be attributed to differences between the present idealized geometry and the experimental configuration of the benchmark study, as well as variations in boundary condition implementation, particularly the inlet waveform scaling and outlet impedance modeling.

Overall, the close agreement in both velocity- and wall shear stress-based metrics demonstrates that the solver configuration, boundary condition treatment, and viscosity modeling strategy employed in this study are sufficient to accurately resolve unsteady inertial effects and near-wall hemodynamics in carotid bifurcations.

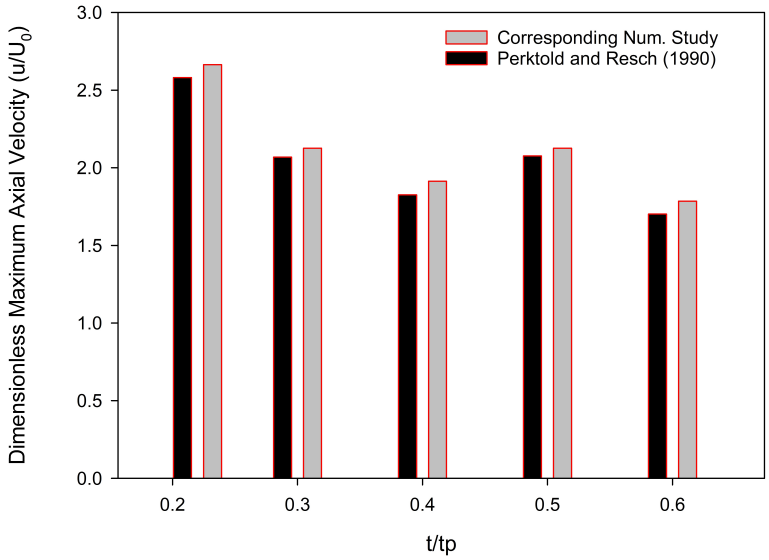


Figure 6. Comparison of the nondimensional maximum axial velocity between the present numerical model and the benchmark data of Perktold and Resch [37] at point D_m. The abscissa represents the normalized time t/t_p, where t is the physical time and t_p denotes the cardiac cycle period. The axial velocity is nondimensionalized using the mean inlet velocity U_0 as the reference scale.

3. Results and Discussion

3.1. Flow Field and Streamline Distribution

Figures 7–10 present the instantaneous streamline and velocity fields at peak systole ($t = 0.22$ s) for the four bifurcation geometries (A–D) under the three MCV-dependent viscosity conditions (70, 90, and 110 fL). The color contours illustrate the velocity magnitude, while the streamlines depict the spatial organization of the flow, including jet coherence, secondary motion, and recirculation regions within the bifurcation. Here, jet coherence refers to the axial persistence of the high-velocity core, quantified by the downstream extent of regions exceeding approximately 80% of the peak velocity, while secondary motion and recirculation are inferred from the spatial spread and density of streamlines in cross-sectional planes. Across all cases, the overall flow topology is primarily governed by the bifurcation angle, whereas MCV-dependent viscosity variations introduce secondary modulation by altering jet thickness, shear layer development, and the axial length of the high-velocity core. These qualitative flow features provide the physical basis for the quantitative hemodynamic metrics discussed in the subsequent sections.

The numerical integrity of the current CFD framework is substantiated by comparing the computed velocity fields and streamline topologies with established literature on carotid hemodynamics. At peak systole ($t = 0.22$ s), the transition from a coherent jet in narrow-angle configurations (Geometry A) to a separation-dominated regime in wide-angle configurations (Geometry D) aligns with the fundamental experimental observations of Ku et al. [38] and Mokhtari et al. [39]. Specifically, the measured peak velocities across the geometries (0.471 to 0.539 m/s, as shown in Figures 7–10) fall within the physiologically expected range for healthy and moderately dilated bifurcations under pulsatile conditions.

The validation is further reinforced by the captured secondary flow structures. In Geometry A, the sustained jet penetration ($L_j \approx 2.5D$) and the absence of large-scale recirculation zones reflect the high-momentum coherence typically reported for streamlined bifurcations. Conversely, the early jet breakdown observed in Geometry D ($L_j < 1.0D$), characterized by significant transverse dispersion and the emergence of stable vortical structures in the frontal cross-sectional planes (Figure 10d–f), accurately replicates the

curvature-induced separation patterns documented in validated numerical studies of aortic and carotid bifurcations [10,37,40,41]. This topological agreement, combined with the consistent response of TAWSS and OSI to geometric divergence (Figures 11 and 12), ensures that the current model effectively captures the essential physics of internal carotid artery hemodynamics.

3.2. Comparative Flow Topology and Quantitative Jet Dynamics

Figures 7–10 illustrate the peak-systolic flow field ($t = 0.22$ s), where a clear transition from a jet-dominated to a recirculation-dominated regime is observed as the bifurcation angle increases. To support these qualitative observations, we define the jet penetration length (L_j) as the axial distance from the apex to the point where the centerline velocity drops below 50% of the peak inlet velocity.

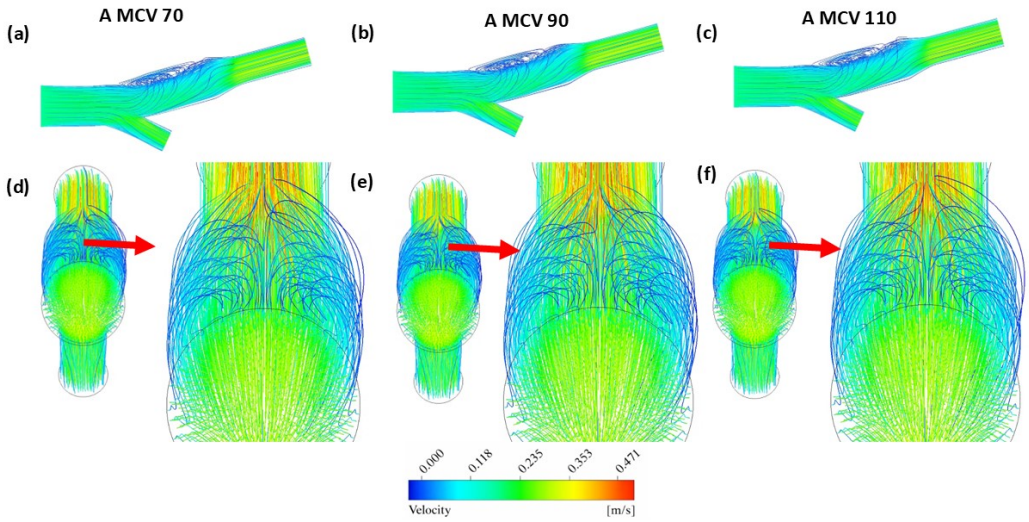


Figure 7. Instantaneous streamlines and velocity magnitude for Geometry A (40°) at peak systole ($t = 0.22$ s) for MCV = 70, 90, and 110 fL: (**a**–**c**) side views; (**d**–**f**) frontal cross-sections. Red arrows indicate the primary flow-separation/recirculation (secondary-vortex) region downstream of the bifurcation apex (outer-wall side), highlighted to facilitate comparison among MCV cases.

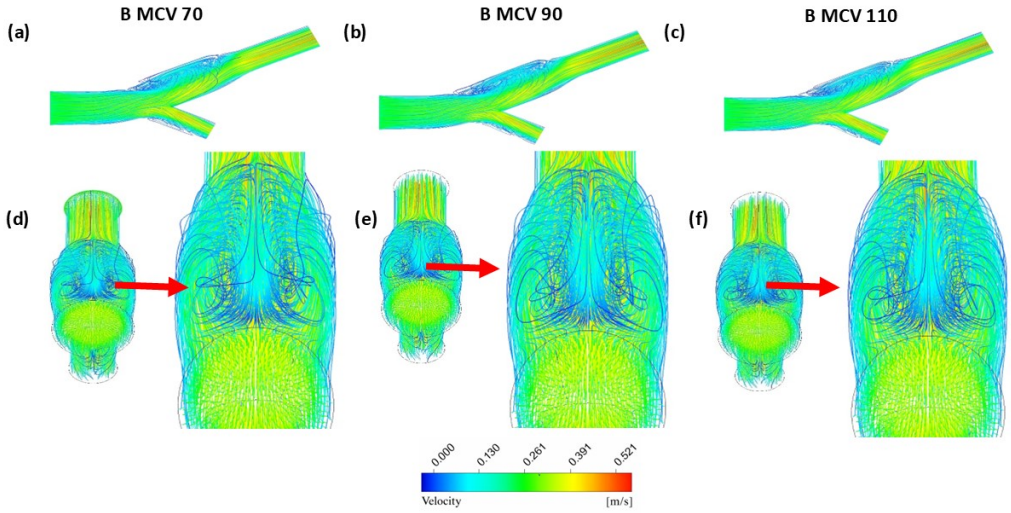


Figure 8. Instantaneous streamlines and velocity magnitude for Geometry B (50°) at peak systole ($t = 0.22$ s) for MCV = 70, 90, and 110 fL: (**a**–**c**) side views; (**d**–**f**) frontal cross-sections. Red arrows indicate the primary flow-separation/recirculation (secondary-vortex) region downstream of the bifurcation apex (outer-wall side), highlighted to facilitate comparison among MCV cases.

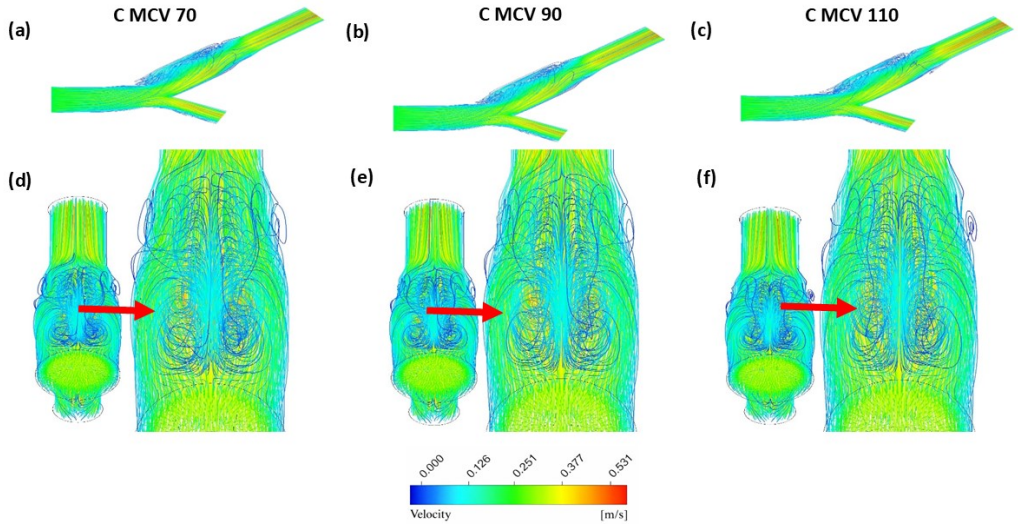


Figure 9. Instantaneous streamlines and velocity magnitude for Geometry C (65°) at peak systole ($t = 0.22$ s) for MCV = 70, 90, and 110 fL: (**a**–**c**) side views; (**d**–**f**) frontal cross-sections. Red arrows indicate the primary flow-separation/recirculation (secondary-vortex) region downstream of the bifurcation apex (outer-wall side), highlighted to facilitate comparison among MCV cases.

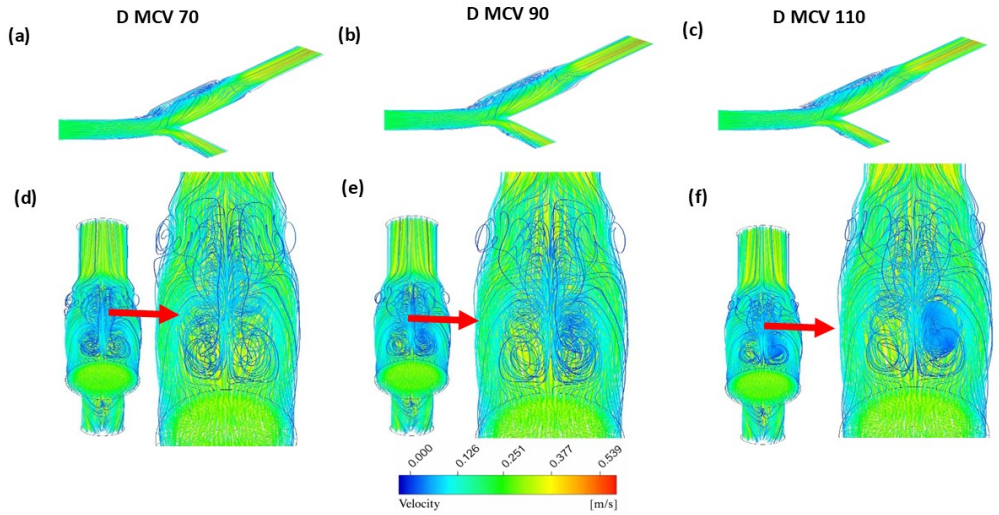


Figure 10. Instantaneous streamlines and velocity magnitude for Geometry D (100°) at peak systole ($t = 0.22$ s) for MCV = 70, 90, and 110 fL: (**a**–**c**) side views; (**d**–**f**) frontal cross-sections. Red arrows indicate the primary flow-separation/recirculation (secondary-vortex) region downstream of the bifurcation apex (outer-wall side), highlighted to facilitate comparison among MCV cases.

3.2.1. Regime Transitions and Velocity Decay

The bifurcation angle is the primary determinant of momentum preservation. In the narrowest configuration (Geometry A, 40°), the axial alignment maintains a high-velocity core that extends significantly into the daughter branches. Specifically, at MCV = 70 fL, the jet core exhibits a peak velocity of ∼0.47 m/s with a penetration length L_j approximately 2.5 times the vessel diameter (D).

As the angle widens to 100° (Geometry D), the rapid geometric expansion triggers an immediate velocity decay. In this configuration, the peak core velocity is attenuated by approximately 15–20% compared to Geometry A, and the jet penetration L_j is reduced to less than 1.0 D. This quantitative decay confirms the early jet breakdown observed in Figure 10a–c.

3.2.2. Quantitative Impact of *MCV*-Dependent Viscosity

The modulation provided by *MCV* (70 to 110 fL) is most evident in the shear layer thickness and vortex stability. As summarized quantitatively in Table 3, variations in vessel angulation lead to systematic changes in peak velocity, jet penetration length, and flow regime classification at peak systole.

- **Momentum Diffusion:** Increasing *MCV* from 70 to 110 fL results in a systematic broadening of the velocity profile. In Geometry C, this leads to a ∼12% increase in the cross-sectional area occupied by low-velocity flows ($u < 0.1$ m/s) near the outer wall.
- **Vortical Activity:** In Geometry D, the higher effective viscosity at 110 fL stabilizes the separated regions, leading to a more diffuse but spatially persistent recirculation zone compared to the higher-velocity, more transient vortices seen at 70 fL.

Table 3. Quantitative Flow Parameters at Peak Systole (*MCV* = 70 fL).

Configuration	Peak Velocity [m/s]	Jet Penetration (L_j/D)	Flow Regime
Geometry A (40°)	0.471	∼2.5	Attached
Geometry B (50°)	0.521 *	∼2.1	Transitional
Geometry C (65°)	0.531 *	∼1.6	Partially Separated
Geometry D (100°)	0.539 *	∼0.9	Fully Separated

* Note: Higher peak values in wider angles often indicate localized acceleration due to stronger jet impingement on the outer wall before rapid decay.

Flow Physics Interpretation: Vortex Dynamics, Jet Breakdown, and Recirculation Mechanisms

Across all geometries, the observed streamline patterns reveal consistent flow-physics mechanisms that explain how both bifurcation angle and *MCV*-dependent viscosity shape the three-dimensional vortex structures. The organization of secondary vortices, separation length, and recirculation intensity is primarily governed by the evolution of three fundamental features: (i) the axial jet issuing from the common carotid artery, (ii) the shear layer formed between the jet core and the near-wall region, and (iii) curvature- and angle-induced secondary vortical motion.

In narrow geometries (40–50°), the momentum of the incoming jet is preserved due to the small divergence angle, which minimizes the adverse pressure gradient along the outer curvature. As a result, flow separation is weak and the shear layer remains thin and stable, preventing the formation of large-scale recirculation. Vortical activity is limited to small, geometrically induced secondary flows near the divider, consistent with stable Dean-type structures.

As the bifurcation angle widens (65–100°), the rapid geometric expansion generates a strong adverse pressure gradient that promotes early jet detachment from the outer wall. This detachment initiates a distinct recirculation bubble whose size increases with angle. The shear layer separating the jet from the near-wall region thickens and becomes more unstable, giving rise to asymmetric vortex structures and low-momentum zones that extend downstream into the external carotid branch.

The influence of viscosity manifests primarily through modulation of these existing topological features rather than altering the topology itself. Higher *MCV* (and therefore higher viscosity) enhances momentum diffusion, which: (i) dampens the axial jet more rapidly, (ii) stabilizes vortical structures by reducing local shear-layer instabilities, and (iii) enlarges recirculation regions by promoting energy dissipation within low-momentum zones. This effect is most evident in wide-angle geometries where the flow is predisposed to separation; here viscosity amplifies the size, coherence, and persistence of the vortices.

Overall, the interplay between jet breakdown, shear-layer behavior, and curvature-induced secondary motion explains the observed *MCV*-dependent differences in recirculation and vortex organization. The addition of viscosity-dependent scaling modifies the strength and extent of separated regions, while the branching angle determines whether these modifications remain subtle (narrow geometries) or become dominant features of the velocity field (wide-angle geometries).

3.3. Comparative Analysis of Geometry and MCV Effects

A comparative examination of Figures 7–10 highlights the coupled influence of bifurcation geometry and *MCV*-dependent viscosity on the organization of the velocity field. Narrow-angle configurations (Geometries A–B, 40–50°) preserve a largely axially aligned flow structure and sustain a coherent jet that transitions smoothly into the daughter branches with limited flow separation. In contrast, wider configurations (Geometries C–D, 65–100°) introduce pronounced geometric divergence, which promotes earlier jet diffusion, enhanced secondary motion, and the development of extended recirculation zones. As *MCV* increases from 70 to 110 fL, the associated rise in effective viscosity leads to progressive momentum diffusion, reducing jet sharpness and strengthening viscosity-sensitive flow features, particularly in regions governed by curvature and branch expansion.

In Geometry A, the confined bifurcation angle suppresses large-scale separation and maintains a stable streamline organization across all *MCV* levels. Variations in viscosity primarily affect the penetration length of the jet core and the thickness of the near-wall shear layer, without substantially altering the global flow topology. Geometry B introduces curvature-induced asymmetry, where increasing *MCV* results in a shorter and thicker velocity core accompanied by more localized and stable streamline curvature within the recirculating region near the bifurcation apex. Geometry C exhibits a more evident redistribution of momentum between branches, with the external carotid artery receiving a weaker and more diffusely organized portion of the inlet jet as viscosity increases. Geometry D displays the strongest geometric influence, characterized by rapid axial momentum decay, early jet breakdown, and persistent recirculation along the outer curvature that becomes increasingly stable under higher-viscosity conditions.

A key observation emerging from these comparisons is that the bifurcation angle dictates the overall flow topology, while viscosity modulates the intensity and spatial extent of existing flow features rather than fundamentally altering their structure. Wider angles inherently generate stronger adverse pressure gradients and larger separated regions, which dominate the distribution of velocity, shear, and residence time. Viscosity acts primarily through uniform momentum diffusion, and its relative influence therefore remains secondary to that of geometric divergence, which directly reorganizes the flow into distinct jet, shear-layer, and recirculation zones. This behavior explains why *MCV*-dependent effects are modest in narrow geometries but become increasingly apparent in wide-angle configurations that are intrinsically prone to instability and separation. Similar dominance of geometric factors has been reported in previous carotid CFD investigations, where vascular morphology accounted for the majority of variability in WSS-based indices, while rheological properties introduced secondary modulation [2,4,6].

Overall, increasing *MCV* enhances viscous diffusion and progressively broadens the low-velocity regions surrounding the jet core, while wider bifurcation angles amplify flow separation and stabilize recirculating structures. Streamline clustering within these separated zones reflects reduced axial transport and prolonged local residence times under higher-viscosity conditions. Narrow configurations maintain coherent, well-organized flow with minimal secondary motion, whereas wide-angle bifurcations exhibit a pronounced

interaction between geometry and viscosity that governs the spatial distribution of velocity and shear-related flow characteristics.

3.4. Quantitative Evaluation of Hemodynamic Indices (TAWSS, OSI, and RRT)

Figures 11–13 illustrate the spatial distribution of these indices for all geometries and *MCV* groups. Since each index is computed as a temporal integral followed by a surface integral, the resulting values reflect the combined temporal stability and spatial organization of shear. Consequently, variations in *MCV*-induced viscosity or bifurcation angle manifest primarily through changes in separation strength, recirculation extent, and near-wall shear reversal.

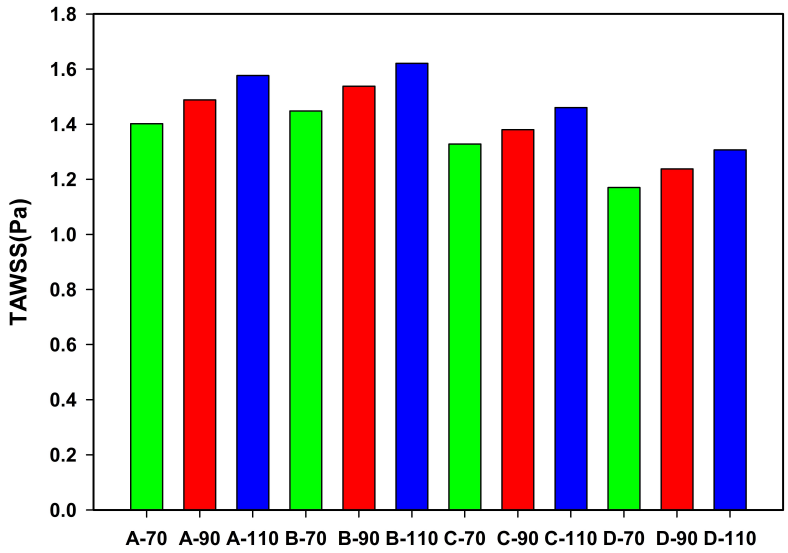


Figure 11. Comparison of time-averaged wall shear stress (TAWSS) for Geometries A–D at different mean corpuscular volume (*MCV*) levels. Green, red, and blue bars correspond to *MCV* values of 70 fL, 90 fL, and 110 fL, respectively. The combined effects of viscosity variation and bifurcation angle lead to a pronounced increase in flow unsteadiness.

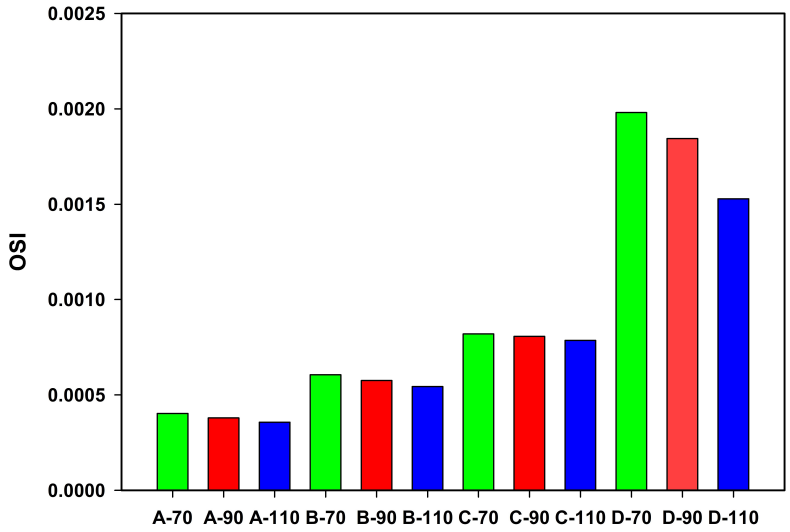


Figure 12. Comparison of oscillatory shear index (OSI) for Geometries A–D at different *MCV* values. Green, red, and blue bars correspond to *MCV* values of 70 fL, 90 fL, and 110 fL, respectively. The combined effect of viscosity and bifurcation angle significantly increases flow unsteadiness.

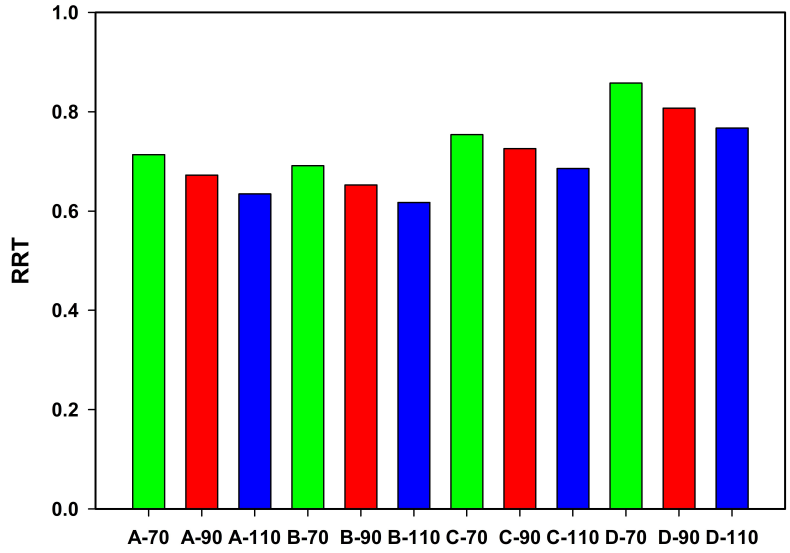


Figure 13. Comparison of relative residence time (RRT) for Geometries A–D at different *MCV* values. Green, red, and blue bars correspond to *MCV* values of 70 fL, 90 fL, and 110 fL, respectively. The combined effect of viscosity and bifurcation angle significantly increases flow unsteadiness.

3.4.1. TAWSS Behavior Across Geometries

In the narrowest configuration (Geometry A), TAWSS exhibits the highest values across all *MCV* levels, indicating a predominantly axial and well-organized flow structure that sustains strong near-wall velocity gradients. Increasing *MCV* from 70 to 110 fL results in a monotonic increase in TAWSS, reflecting enhanced shear generation associated with increased volumetric flow.

In Geometry B, TAWSS remains comparable to Geometry A but shows slightly reduced magnitudes due to the onset of geometric divergence. Nevertheless, TAWSS increases consistently with *MCV*, suggesting that inertial strengthening dominates over viscous diffusion within this angular range.

Geometry C demonstrates a further reduction in TAWSS as the bifurcation angle increases, promoting flow separation and redistribution of momentum away from the wall. Although TAWSS continues to increase with *MCV*, its absolute magnitude remains lower than that observed in Geometries A and B, indicating weakened near-wall velocity gradients induced by secondary flow structures.

The widest configuration (Geometry D) exhibits the lowest TAWSS values among all cases. Strong geometric divergence leads to early jet breakdown and flow separation, substantially attenuating wall shear despite increasing *MCV*. These findings indicate that geometric spreading governs the reduction of time-averaged wall shear in highly divergent configurations.

Overall, TAWSS decreases systematically with an increasing bifurcation angle, while *MCV* primarily modulates shear magnitude within a given geometry.

3.4.2. OSI and RRT Behavior Across Geometries

At the outset, it should be emphasized that oscillatory shear index (OSI) values are expected to remain relatively low in laminar Newtonian flow regimes, particularly in large-artery configurations where flow reversal is spatially localized and temporally limited [42,43]. Under such conditions, OSI primarily captures localized oscillations associated with flow separation and recirculation rather than global oscillatory behavior of the wall shear stress field. Accordingly, the interpretation of OSI in this study focuses on relative spatial and parametric variations rather than on absolute magnitude.

OSI and RRT exhibit consistent and physically meaningful trends across all geometries. In Geometry A, both indices remain minimal at all *MCV* levels, confirming the absence of significant flow reversal or oscillatory wall shear. Increasing *MCV* slightly reduces OSI and RRT, indicating enhanced flow stability under higher volumetric conditions.

Geometry B shows moderately higher OSI and RRT values compared to Geometry A, reflecting the emergence of weak secondary motion induced by geometric divergence. Both indices decrease with increasing *MCV*, suggesting that strengthened convective transport suppresses oscillatory shear and reduces near-wall residence time.

In Geometry C, OSI and RRT increase further due to more extensive flow separation and recirculation near the outer wall. The highest values are observed at lower *MCV*, while increasing *MCV* progressively reduces both indices, indicating stabilization of separated flow structures under stronger inertial forcing.

Geometry D exhibits the largest OSI and RRT magnitudes across all configurations, reflecting pronounced recirculation and low-velocity regions caused by strong geometric divergence. Nevertheless, both indices decrease systematically with increasing *MCV*, demonstrating that increased volumetric capacity mitigates oscillatory behavior and shortens residence time even in highly disturbed flows.

Across all cases, OSI and RRT increase with bifurcation angle and decrease with *MCV*, highlighting the dominant role of geometry in generating disturbed flow and the stabilizing influence of increased volumetric flow.

3.4.3. Numerical Considerations

Although OSI is known to be sensitive to numerical resolution, the observed differences between geometries exhibit clear separation, indicating that the dominant trends are physically driven rather than numerical artifacts. Minor variations between *MCV* levels may fall within numerical tolerance; however, the consistent monotonic behavior across all configurations suggests that geometry primarily governs oscillatory shear patterns, while *MCV* acts as a secondary stabilizing factor. This behavior is consistent with previous studies reporting stronger geometric control over OSI compared to viscosity-related effects.

3.5. Statistical Sensitivity Analysis of Geometry–MCV Interaction

The numerical results demonstrate that both bifurcation geometry and *MCV*-dependent viscosity exert systematic but distinct influences on carotid hemodynamics within the deterministic CFD framework considered in this study. Narrow-angle configurations (Geometries A and B) promote predominantly axial inflow with limited flow separation, resulting in stable wall shear patterns and weak oscillatory behavior. In contrast, wide-angle geometries (Geometries C and D) induce strong geometric divergence, promoting flow separation, recirculation, and increased spatial heterogeneity of near-wall hemodynamic indices.

To quantify the relative importance of these effects, a two-way factorial analysis of variance (ANOVA) was employed as a deterministic sensitivity analysis tool, with geometry (A–D) and *MCV* group (70–110 fL) treated as fixed input factors and surface-averaged TAWSS, OSI, and RRT as model outputs. In this context, the ANOVA does not represent population-level statistical inference, but rather provides a structured variance decomposition to assess the relative contribution and interaction strength of the governing model parameters.

As summarized in Table 4, geometric configuration accounts for the dominant share of variability across all hemodynamic indices, confirming that structural divergence is the primary determinant of near-wall flow behavior in the simulated carotid bifurcation. *MCV*-dependent viscosity introduces a secondary but statistically significant contribu-

tion, while the interaction term indicates that the influence of *MCV* is modulated by geometric configuration.

Specifically, in narrow-angle geometries (A–B), increased *MCV* primarily strengthens axial momentum transport and stabilizes wall shear, leading to moderate changes in TAWSS and reduced oscillatory metrics. In wide-angle configurations (C–D), where flow separation and recirculation dominate the near-wall environment, the sensitivity of TAWSS, OSI, and RRT to *MCV* is attenuated, as geometric effects overwhelm viscosity-driven modulation.

Table 4. Two-way factorial sensitivity analysis quantifying the relative contributions of geometry, *MCV*-dependent viscosity, and their interaction to deterministic hemodynamic outputs.

Factor	TAWSS (F, *p*)	OSI (F, *p*)	RRT (F, *p*)
Geometry (A–D)	182.6, <0.001	241.3, <0.001	228.7, <0.001
MCV (70–110 fL)	21.4, 0.001	17.2, 0.002	18.9, 0.002
Geometry × *MCV*	6.8, 0.011	7.5, 0.009	8.1, 0.008

Interpretation: Within the deterministic setting of the present CFD simulations, these results demonstrate that geometry governs the formation and spatial extent of disturbed flow, while *MCV*-dependent viscosity acts as a secondary modulating parameter that primarily stabilizes near-wall shear and reduces oscillatory behavior. Accordingly, the reported F-statistics should be interpreted as indicators of relative parameter sensitivity within the numerical model rather than as measures of experimental variability or population-level statistical significance.

Physiological Interpretation and Literature Consistency

The geometry-dependent modulation of TAWSS, OSI, and RRT observed in this study is consistent with existing computational and experimental findings. Previous work by Morbiducci et al. [3] and Gallo et al. [44] demonstrated that geometric divergence is the primary driver of wall shear heterogeneity, while blood viscosity plays a secondary role by modulating the intensity and temporal character of disturbed flow. Similarly, Peiffer et al. [45] reported that geometry-induced secondary vortices govern the spatial extent of oscillatory shear, with viscosity influencing their stability rather than their formation.

Within this framework, the present results indicate that variations in *MCV*, modeled through an effective Newtonian viscosity, exert a stabilizing influence on near-wall hemodynamics, particularly in geometries characterized by predominantly axial inflow (Geometries A and B). In these configurations, increased viscosity enhances momentum diffusion and suppresses oscillatory shear components. In contrast, in highly divergent geometries (Geometries C and D), where flow separation and recirculation are primarily governed by structural features, the influence of viscosity on TAWSS, OSI, and RRT is attenuated, as geometric effects dominate the local hemodynamic environment.

These findings support the view that patient-specific variability in blood viscosity can modulate local shear conditions, but its impact remains secondary to vascular geometry in determining the overall hemodynamic landscape. This interpretation is in line with prior studies emphasizing geometry as the principal determinant of disturbed flow patterns in arterial bifurcations.

3.6. Model Assumptions and Limitations

The present study provides a controlled numerical assessment of the influence of *MCV*-dependent viscosity on carotid bifurcation hemodynamics; however, several modeling assumptions introduce inherent limitations that should be considered when interpreting the results.

First, blood was modeled as a Newtonian fluid with an *MCV*-based effective viscosity. This formulation neglects shear-dependent rheological behavior and the nonlinear interaction between shear rate, hematocrit, and erythrocyte deformability, particularly in low-shear regions. As a consequence, shear-thinning effects are not captured, which may

influence the absolute magnitude of TAWSS and smooth the spatial distribution of OSI and RRT. This simplification was intentionally adopted to isolate the first-order sensitivity of hemodynamic indices to *MCV* variation, such that relative trends across geometries and viscosity groups remain interpretable within a deterministic framework.

Second, arterial walls were assumed to be rigid and fluid–structure interaction was not considered. Wall compliance may attenuate peak systolic velocities and reduce oscillatory shear near the bifurcation apex. Accordingly, the reported OSI and RRT values may represent upper-bound estimates under rigid-wall conditions, while comparative differences across geometries and *MCV* levels are expected to remain robust.

Third, although physiologically realistic outlet behavior was incorporated through a three-element Windkessel (RCR) model to represent downstream vascular impedance, the parameters were not patient-specific. While the Windkessel formulation enables more realistic pressure–flow coupling compared with fixed-pressure outlets, subject-specific impedance variations may alter local flow partitioning and the absolute magnitude of wall shear metrics.

Fourth, idealized bifurcation geometries were employed, neglecting patient-specific features such as vessel tortuosity, asymmetric branch diameters, and secondary curvature. This simplification may limit the spatial specificity of predicted low-TAWSS and high-OSI regions, but it enables controlled attribution of observed hemodynamic changes to geometric divergence and viscosity modulation without confounding anatomical variability.

Finally, model validation was conducted against well-established benchmark velocity and wall shear stress data reported in the literature. While this comparison supports the physical realism and numerical consistency of the present predictions, direct in vivo validation using subject-specific measurements was beyond the scope of the study.

Future work should incorporate non-Newtonian rheology, compliant vessel walls, patient-specific geometries, and personalized boundary conditions to further quantify the role of *MCV* in arterial hemodynamics under fully physiological conditions.

4. Conclusions

This study introduced a simplified *MCV*-dependent effective viscosity framework to examine how hematological variability influences carotid bifurcation hemodynamics under pulsatile Newtonian flow conditions. The results demonstrate that *MCV*-related changes in viscosity primarily modulate shear-based indices through their interaction with geometric divergence and flow separation mechanisms. While narrow-angle configurations maintain largely coherent and stable flow structures, viscosity variations influence local jet thickness and near-wall shear-layer development. In contrast, wider bifurcations with pronounced recirculation exhibit a stronger sensitivity to *MCV*, where increased viscosity enhances momentum diffusion, stabilizes separated flow regions, and alters the spatial distribution of wall shear.

Overall, the findings confirm that vascular geometry governs the dominant flow topology and the formation of disturbed flow regions, whereas *MCV*-dependent viscosity acts as a secondary modulating factor whose impact is strongly geometry-dependent rather than uniform across the bifurcation. This hierarchy is consistently reflected in the streamline organization as well as in WSS-based metrics, including TAWSS, OSI, and RRT.

From a methodological perspective, the proposed viscosity-scaling approach offers a practical means of incorporating routinely measured hematological parameters into CFD simulations without introducing the additional complexity of fully shear-dependent rheological models. This strategy enables a physiologically motivated representation of inter-individual variability in blood properties while preserving the numerical robustness and computational efficiency of Newtonian flow formulations. In this context, the proposed

MCV-dependent viscosity framework can be directly extended toward patient-specific CFD and digital twin applications by integrating medical imaging-derived vascular geometries and individualized hematological and physiological parameters, enabling personalized assessment of carotid hemodynamics under subject-specific conditions.

Author Contributions: Conceptualization, A.Ç.; methodology, A.Ç.; software, A.Ç.; validation, A.Ç.; formal analysis, A.Ç.; investigation, A.Ç.; resources, Ö.Ç. and M.İ.; data curation, A.Ç.; writing—original draft preparation, A.Ç.; writing—review and editing, A.Ç., H.B., Ö.Ç. and M.İ.; visualization, H.B. and A.Ç.; supervision, Ö.Ç. and M.İ. All authors have read and agreed to the published version of the manuscript.

Funding: This research received no external funding. The study was conducted without financial support from any funding agency. The APC was not funded.

Institutional Review Board Statement: Not applicable. The study did not involve humans or animals.

Informed Consent Statement: Not applicable. This numerical simulation study did not involve human participants or identifiable patient data, and therefore informed consent for publication was not required.

Data Availability Statement: The original contributions presented in the study are included in the article, further inquiries can be directed to the corresponding author.

Acknowledgments: During the preparation of this manuscript, the authors used OpenAI ChatGPT (GPT-5, October 2025 release) for improving grammar and clarity. The authors have reviewed and edited the AI-generated text and take full responsibility for the final content of this publication.

Conflicts of Interest: The authors declare no conflict of interest.

Abbreviations

The following abbreviations are used in this manuscript:

Abbreviation	Definition
MCV	Mean Corpuscular Volume
Hct	Hematocrit
RBC	Red Blood Cell
WSS	Wall Shear Stress
TAWSS	Time-Averaged Wall Shear Stress
OSI	Oscillatory Shear Index
RRT	Relative Residence Time
CCA	Common Carotid Artery
ICA	Internal Carotid Artery
ECA	External Carotid Artery
UDF	User-Defined Function
CFD	Computational Fluid Dynamics
FSI	Fluid–Structure Interaction
LES	Large Eddy Simulation
RCR	Resistance–Compliance–Resistance (Windkessel) Model
μ	Dynamic Viscosity
ρ	Density
Re	Reynolds Number
t/t_p	Non-dimensional Time Ratio
μ_{p0}	Plasma Viscosity
η_{rel}	Relative Viscosity
k_0	Reference Quemada Constant
c_3	Empirical Sensitivity Coefficient
μ_{eff}	Effective Viscosity

References

1. Campbell, I.C.; Ries, J.; Dhawan, S.S.; Quyyumi, A.A.; Taylor, C.A.; Oshinski, J.N. Effect of Inlet Velocity Profiles on Patient-Specific Carotid Bifurcation Hemodynamics. *J. Biomech. Eng.* **2012**, *134*, 051001. [CrossRef] [PubMed]
2. Moyle, K.R.; Antiga, L.; Steinman, D.A. Inlet Conditions for Image-Based CFD Models of the Carotid Bifurcation: Is It Reasonable to Assume Fully Developed Flow. *J. Biomech. Eng.* **2006**, *128*, 371–379. [CrossRef] [PubMed]
3. Morbiducci, U.; Ponzini, R.; Gallo, D.; Bignardi, C.; Rizzo, G. Inflow Boundary Conditions for Image-Based Computational Hemodynamics: Impact of Secondary Flows at Inlet on Wall Shear Stress. *J. Biomech. Eng.* **2010**, *132*, 114501. [CrossRef]
4. Lee, S.W.; Antiga, L.; Spence, J.D.; Steinman, D.A. Geometry of the Carotid Bifurcation Predicts Its Exposure to Disturbed Flow. *Stroke* **2008**, *39*, 2341–2347. [CrossRef]
5. Peiffer, V.; Sherwin, S.J.; Weinberg, P.D. Computation in the rabbit aorta of a new metric—The transverse wall shear stress—To quantify the multidirectional character of disturbed blood flow. *J. Biomech.* **2013**, *46*, 2651–2658. [CrossRef]
6. Steinman, D.A.; Taylor, C.A. Flow imaging and computing: Large artery hemodynamics. *Ann. Biomed. Eng.* **2005**, *33*, 1704–1709. [CrossRef]
7. Strecker, C.; Krafft, A.J.; Kaufhold, L.; Hüllebrandt, M.; Treppner, M.; Ludwig, U.; Köber, G.; Hennemuth, A.; Hennig, J.; Harloff, A. Carotid Geometry and Wall Shear Stress Independently Predict Increased Wall Thickness—A Longitudinal 3D MRI Study in High-Risk Patients. *Front. Cardiovasc. Med.* **2021**, *8*, 723860. [CrossRef]
8. Gharahi, H.; Zambrano, B.A.; Zhu, D.C.; DeMarco, J.K.; Baek, S. Computational fluid dynamic simulation of human carotid artery bifurcation based on anatomy and volumetric blood flow rate measured with magnetic resonance imaging. *Int. J. Adv. Eng. Sci. Appl. Math.* **2016**, *8*, 40–60. [CrossRef]
9. Antiga, L.; Steinman, D.A. Robust and objective decomposition and mapping of bifurcating vessels. *IEEE Trans. Med. Imaging* **2008**, *27*, 1688–1698. [CrossRef]
10. Lee, S.-W.; Steinman, D.A. On the relative importance of rheology for image-based CFD models of the carotid bifurcation. *J. Biomech. Eng.* **2007**, *129*, 273–278. [CrossRef]
11. Markl, M.; Wallis, W.; Brendecke, S.; Simon, J.; Frydrychowicz, A.; Harloff, A. Analysis of 3-D Blood Flow Dynamics in the Carotid Artery by Flow-Sensitive Four-Dimensional MRI: Impact of Carotid Geometry and Atherosclerosis in Mild to Moderate Stenosis. *Circ. Cardiovasc. Imaging* **2010**, *3*, 550–557. [CrossRef]
12. Chien, S. Shear Dependence of Effective Cell Volume as a Determinant of Blood Viscosity. *Science* **1970**, *168*, 977–979. [CrossRef] [PubMed]
13. Skalak, R.; Brånemark, P. Deformation of Red Blood Cells in Capillaries. *Science* **1969**, *164*, 717–719. [CrossRef] [PubMed]
14. Popel, A.S.; Johnson, P.C. Microcirculation and hemorheology. *Annu. Rev. Fluid Mech.* **2005**, *37*, 43–69. [CrossRef]
15. Sunderland, K.; Jiang, J.; Zhao, F. Disturbed flow's impact on cellular changes indicative of vascular aneurysm initiation, expansion, and rupture: A pathological and methodological review. *J. Cell. Physiol.* **2021**, *237*, 278–300. [CrossRef]
16. Ekmejian, A.; Carpenter, H.; Ciofani, J.; Gray, B.; Allahwala, U.; Ward, M.; Escaned, J.; Psaltis, P.; Bhindi, R. Advances in the Computational Assessment of Disturbed Coronary Flow and Wall Shear Stress: A Contemporary Review. *J. Am. Heart Assoc.* **2024**, *13*, e037129. [CrossRef]
17. Hernández-López, P.; Cilla, M.; Martínez, M.; Peña, E.; Malvé, M. Impact of geometric and hemodynamic changes on a mechanobiological model of atherosclerosis. *Comput. Biol. Med.* **2024**, *254*, 108296. [CrossRef]
18. Garcha, A.; Gutierrez, G. Sensitivity of coronary hemodynamics to vascular structure variations in health and disease. *Sci. Rep.* **2025**, *15*, 3325. [CrossRef]
19. Kumar, R.; Muralidhar, K.; Dalal, I.S. Effects of geometric modeling and blood rheology in patient-specific arterial blood flow simulations with speed–accuracy trade-off analysis. *J. Non-Newton. Fluid Mech.* **2026**, *348*, 105534. [CrossRef]
20. Nicoleau, S.; Valle, Y.R.; Tura-Ceide, O.; Armour, C.H.; Barberá, J.A.; McKinnon, T.A.J.; Gopalan, D.; Wojciak-Stothard, B. 3D modelling of pulmonary arterial stenosis and endothelial dysfunction in CTEPH. *Lab A Chip* **2025**, *25*, 4369–4384. [CrossRef]
21. Nisco, G.; Rizzini, M.; Verardi, R.; Chiastra, C.; Candreva, A.; De Ferrari, G.; D'Ascenzo, F.; Gallo, D.; Morbiducci, U. Modelling blood flow in coronary arteries: Newtonian or shear-thinning non-Newtonian rheology? *Comput. Methods Programs Biomed.* **2023**, *242*, 107823. [CrossRef]
22. Chakraborty, S.; Mantripragada, V.; Chakravarty, A.; Goswami, D.; Poddar, A. Unraveling the complex interplay between abnormal hemorheology and shape asymmetry in flow through stenotic arteries. *Comput. Methods Programs Biomed.* **2024**, *257*, 108437. [CrossRef] [PubMed]
23. Wajihah, A.; Sankar, D. A review on non-Newtonian fluid models for multi-layered blood rheology in constricted arteries. *Arch. Appl. Mech.* **2023**, *93*, 1771–1796. [CrossRef] [PubMed]
24. Kandangwa, P.; Torii, R.; Gatehouse, P.; Sherwin, S.; Weinberg, P. Influence of right coronary artery motion, flow pulsatility and non-Newtonian rheology on wall shear stress metrics. *Front. Bioeng. Biotechnol.* **2022**, *10*, 962687. [CrossRef]
25. Javadi, E.; Jamali, S. Hemorheology: The critical role of flow type in blood viscosity measurements. *Soft Matter* **2021**, *17*, 8446–8458. [CrossRef]

26. Singh, D.; Singh, S. Numerical study of the effects of bifurcation angle on hemodynamics during pulsatile flow in a carotid artery bifurcation. *Heat Mass Transf.* **2023**, *60*, 147–165. [CrossRef]
27. Chu, J.; Xiao, L.L.; Lin, C.S.; Liu, S.; Zhang, K.X.; Wei, P. Simulation of Non-Newtonian Blood Flow in Diverging Bifurcated Vessels. *J. Appl. Fluid Mech.* **2024**, *17*, 1204–1216. [CrossRef]
28. Abhilash, H.N.; Yanagita, Y.; Pai, R.; Zuber, M.; Tamagawa, M.; Kamath, G.; Barboza, A.B.V.; Rao, V.R.K.; Khader, S.A. Effect of vascular geometry on haemodynamic changes in a carotid artery bifurcation using numerical simulation. *Clin. Neurol. Neurosurg.* **2024**, *237*, 108153. [CrossRef]
29. Perktold, K.; Peter, R.O.; Resch, M.; Langs, G. Pulsatile non-Newtonian blood flow in three-dimensional carotid bifurcation models: A numerical study of flow phenomena under different bifurcation angles. *J. Biomech.* **1991**, *24*, 409–420. [CrossRef]
30. Fragomeni, C.; Mendolicchio, L.; Oliveto, G.; Longo, F. Newtonian and Non-Newtonian Blood Model: A Comparative Study on Large and Small Vessels. In Proceedings of the International Conference on Modeling and Applied Simulation (MAS), Athens, Greece, 18–20 September 2023; pp. 7–14.
31. Stamou, A.; Papadopoulos, K.; Fotiadis, D.I.; Michalis, L.K.; Giannopoulos, A.A. A Comparison of Newtonian and Non-Newtonian Models in Carotid Artery Plaque Deposition Simulations. *Fluids* **2023**, *8*, 282. [CrossRef]
32. Liu, J.; Yuan, C.; Qiao, Y.; Li, Z.; Song, H. Comparison of Newtonian and non-Newtonian fluid models in blood flow simulation in patients with intracranial arterial stenosis. *Front. Physiol.* **2021**, *12*, 718540. [CrossRef] [PubMed]
33. Johnston, B.M.; Johnston, P.R.; Corney, S.; Kilpatrick, D. Non-Newtonian blood flow in human right coronary arteries: Steady state simulations. *J. Biomech.* **2004**, *37*, 709–720. [CrossRef] [PubMed]
34. Baskurt, O.K.; Meiselman, H.J. Blood rheology and hemodynamics. *Semin. Thromb. Hemost.* **2003**, *29*, 435–450. [CrossRef] [PubMed]
35. Cokelet, G.; Meiselman, H. Rheological comparison of hemoglobin solutions and erythrocyte suspensions. *Science* **1968**, *162*, 275–277. [CrossRef]
36. Bharadvaj, B.K.; Mabon, R.F.; Giddens, D.P. Steady Flow in a Model of the Human Carotid Bifurcation. Part I—Flow Visualization. *J. Biomech.* **1982**, *15*, 349–362. [CrossRef]
37. Perktold, K.; Resch, M. Numerical flow studies in human carotid artery bifurcations: Basic discussion of the geometric factor in atherogenesis. *J. Biomech. Eng.* **1990**, *12*, 111–123. [CrossRef]
38. Ku, D.N.; Giddens, D.P.; Zarins, C.K.; Glagov, S. Pulsatile flow and atherosclerosis in the human carotid bifurcation: Positive correlation between plaque location and low oscillating shear stress. *Arteriosclerosis* **1985**, *5*, 293–302. [CrossRef]
39. Mokhtari, A.; Corso, P.; Jung, B.; Ferrari, L.; Zheng, S.; Obrist, D. Comparison of 4D flow MRI and computational fluid dynamics in carotid models with different stenosis levels. *Comput. Biol. Med.* **2025**, *194*, 110405. [CrossRef]
40. Zhao, S.; Xu, X.Y.; Hughes, A.; Thom, S.; Stanton, A.; Ariff, B.; Long, Q. Blood flow and vessel mechanics in a physiologically realistic model of a human carotid arterial bifurcation. *J. Biomech.* **2000**, *33*, 975–984. [CrossRef]
41. Perktold, K.; Rappitsch, G. Computer simulation of local blood flow and vessel mechanics in a compliant carotid artery bifurcation model. *J. Biomech.* **1995**, *28*, 845–856. [CrossRef]
42. Krishna, C.V.; Suja, V.C.; Watton, P.; Watton, P.; Arakeri, J.; Gundiah, N. Shear stress rosettes capture the complex flow physics in diseased arteries. *J. Biomech.* **2020**, *104*, 109721. [CrossRef]
43. Pinto, S.; Campos, J.B.L.M. Numerical study of wall shear stress-based descriptors in the human left coronary artery. *Comput. Methods Biomech. Biomed. Eng.* **2016**, *19*, 1443–1455. [CrossRef]
44. Gallo, D.; Steinman, D.A.; Morbiducci, U. Insights into the co-localization of magnitude-based versus direction-based indicators of disturbed shear at the carotid bifurcation. *J. Biomech.* **2016**, *49*, 2413–2419. [CrossRef]
45. Peiffer, V.; Sherwin, S.J.; Weinberg, P.D. Does low and oscillatory wall shear stress correlate spatially with early atherosclerosis? A systematic review. *Cardiovasc. Res.* **2013**, *99*, 242–250. [CrossRef]

Disclaimer/Publisher's Note: The statements, opinions and data contained in all publications are solely those of the individual author(s) and contributor(s) and not of MDPI and/or the editor(s). MDPI and/or the editor(s) disclaim responsibility for any injury to people or property resulting from any ideas, methods, instructions or products referred to in the content.